PHYSICAL PROPERTIES OF A PILOT SAMPLE OF SPECTROSCOPIC CLOSE PAIR GALAXIES AT $z \sim 2$

DAVID R. LAW[1], ALICE E. SHAPLEY[2], JADE CHECLAIR[3], AND CHARLES C. STEIDEL[4]
[1] Space Telescope Science Institute, 3700 San Martin Drive, Baltimore, MD 21218, USA; dlaw@stsci.edu
[2] Department of Physics and Astronomy, University of California, Los Angeles, CA 90095, USA
[3] Dunlap Institute for Astronomy & Astrophysics, University of Toronto, 50 St. George Street, Toronto, ON M5S 3H4, Canada
[4] California Institute of Technology, MS 249-17, Pasadena, CA 91125, USA

ABSTRACT

We use *Hubble Space Telescope* Wide-field Camera 3 rest-frame optical imaging to select a pilot sample of star-forming galaxies in the redshift range $z = 2.00$–2.65 whose multi-component morphologies are consistent with expectations for major mergers. We follow up this sample of major merger candidates with Keck/NIRSPEC long-slit spectroscopy obtained in excellent seeing conditions (FWHM ~ 0.5 arcsec) to obtain Hα-based redshifts of each of the morphological components in order to distinguish spectroscopic pairs from false pairs created by projection along the line of sight. Of the six candidate pairs observed, companions (estimated mass ratios 5:1 and 7:1) are detected for two galaxies down to a 3σ limiting emission-line flux of $\sim 10^{-17}$ erg s^{-1} cm^{-2}. This detection rate is consistent with a $\sim 50\%$ false-pair fraction at such angular separations (1–2 arcsec) and with recent claims that the star formation rate (SFR) can differ by an order of magnitude between the components in such mergers. The two spectroscopic pairs identified have a total SFR, SFR surface densities, and stellar masses consistent on average with the overall $z \sim 2$ star-forming galaxy population.

Key words: galaxies: fundamental parameters – galaxies: high-redshift – galaxies: structure

1. INTRODUCTION

At redshift $z \sim 2$–3, galaxies are growing rapidly and build up a large fraction of their present-day stellar mass (e.g., Reddy et al. 2008). As they grow, the increased stellar mass is thought to stabilize these systems against gravitational instabilities resulting from their large gas fractions (e.g., Kassin et al. 2014; van der Wel et al. 2014), decreasing their formerly high gas-phase velocity dispersions (Law et al. 2007b, 2009; Förster Schreiber et al. 2009; Newman et al. 2013) and causing a morphological transformation from highly irregular clumpy starbursts (e.g., Guo et al. 2012; Law et al. 2012b; van der Wel et al. 2014 and references therein) to the modern-day Hubble sequence (e.g., Papovich et al. 2005; Law et al. 2012a; Conselice 2014).

One mechanism by which such growth occurs is the conversion of massive gas reservoirs into stars. Such star formation is observed to occur at a typical rate of $\sim 30 M_\odot$ yr^{-1} for rest-UV-selected galaxy samples (e.g., Erb et al. 2006; Wuyts et al. 2011), although this star formation rate (SFR) may represent only a small fraction of the gas continually cycling into (e.g., Genzel et al. 2008; Dekel et al. 2009) and out of the galaxies (e.g., Steidel et al. 2010) through large-scale gas flows. Likewise, galaxies also grow through both major (mass ratio 3:1 or lower) and minor (mass ratio 4:1 or higher) mergers with other galaxies. Such events typically contribute both stars and gas, thereby building up the galactic stellar spheroid population and providing fuel for future generations of star formation. The role of mergers and merger-induced star formation compared to in situ star formation in building up the present-day galaxy population has been the subject of considerable debate, with various studies claiming both that mergers are (de Ravel et al. 2009; Puech et al. 2014; Tasca et al. 2014) and are not (Shapiro et al. 2008; Williams et al. 2011; Wuyts et al. 2011; Kaviraj et al. 2013) major drivers of star formation and galactic stellar mass assembly since $z \sim 4$.

Significant effort has therefore been invested both in constraining the evolution of the merger fraction for star-forming galaxies (e.g., Conselice et al. 2008, 2011; Lotz et al. 2008, 2011; Rawat et al. 2008) and in assessing the physical effects of such mergers on the star formation properties of the galaxies (e.g., Law et al. 2007a, 2012b; Lotz et al. 2008; Lee et al. 2013). One method employed by such studies is to use high-resolution imaging to quantify disturbances and irregularities in the surface brightness profile using a variety of non-parametric indices (e.g., Conselice et al. 2000; Lotz et al. 2004; Law et al. 2007a). However, it is often challenging to interpret such indices unambiguously because $z \sim 2$–3 galaxies are intrinsically clumpy and irregular and similar disturbed morphologies can arise both in merging systems and in isolated star-forming galaxies due to internal dynamical instabilities (e.g., Bournaud & Elmegreen 2009; Genzel et al. 2011).

An alternative way of identifying major mergers is to look for close angular pairs ($r \lesssim 50$ kpc, 6 arcsec at $z \sim 2$–3). When the velocity separation between the two components in such a pair is $\lesssim 500$ km s^{-1} (see the discussion by Lin et al. 2004; Lotz et al. 2008), numerical simulations suggest that such systems should predominantly trace major galaxy–galaxy mergers during their first pericentric passage and before final coalescence (Lotz et al. 2008, 2010). Indeed, when merger rates derived from such close pairs (e.g., Bundy et al. 2009; de Ravel et al. 2009; Williams et al. 2011; López-Sanjuan et al. 2013; Tasca et al. 2014) are combined with physically motivated timescales for interaction, the overall agreement on merger rates between different studies is relatively good (Lotz et al. 2011).

One major complication faced by such efforts to constrain the merger rate (and the physical characteristics of the merging galaxies), however, is the incidence of *false* pairs resulting from chance angular alignments of galaxies separated by large cosmological distances. In the absence of kinematic

information, the false morphological pair fraction can be greater than 50% depending on the adopted impact parameter (see, e.g., the discussion by Patton & Atfield 2008; Quadri & Williams 2010; Chou et al. 2012; Law et al. 2012b) and whether or not photometric redshift selection techniques (e.g., Kartaltepe et al. 2007; Bundy et al. 2009) can be used to help trim the list of potential companions. Although corrections for the false-pair contribution can also be estimated statistically, such statistical corrections do not identify *which* are the true physical pairs, leading to substantial uncertainty in the derived properties of major mergers as a galaxy class.

In a recent contribution (Law et al. 2012b) we used *Hubble Space Telescope* (*HST*) imaging data to quantify the major merger fraction in rest-UV-selected ($\mathcal{R} \leqslant 25.5$)[5] star-forming galaxies at $z \sim 2$–3 using rest-frame optical morphology. Consistent with studies of similar galaxy samples in the literature (e.g., Conselice et al. 2011), we found that $23^{+7}_{-6}\%$ of these galaxies in the redshift range $2.0 < z < 2.5$ were apparent morphological pairs with physical separations of $\leqslant 16$ kpc (~ 2 arcsec), and $16^{+7}_{-6}\%$ were statistically likely to be genuine physical pairs. At such small separations, the pair morphology would not be apparent in the ground-based imaging that forms the backbone of our star-forming galaxy sample.

Here, we follow up the morphological pair sample presented by Law et al. (2012b) with rest-frame optical spectroscopy to determine which of the apparent pairs have similar spectroscopic redshifts suggesting that are likely to coalesce within the next ~ 500 Myr (see Table 5 of Lotz et al. 2010) and to identify whether or not these spectroscopically confirmed pairs have physical characteristics that are any different from those of the rest of the star-forming galaxy population.

We give an overview of the parent galaxy sample in Section 2 and describe the Keck/NIRSPEC spectroscopic follow-up observations targeting rest-optical nebular emission lines in Section 3. In Section 4, we present our results for individual galaxies and discuss the implications of these results for the physical characteristics of genuine merging pairs in Section 5. Throughout our analysis, we adopt a standard ΛCDM cosmology based on the seven-year *WMAP* results (Komatsu et al. 2011) in which $H_0 = 70.4 \text{ km s}^{-1} \text{ Mpc}^{-1}$, $\Omega_M = 0.272$, and $\Omega_\Lambda = 0.728$.

2. TARGET GALAXY SAMPLE

Targets were drawn from the Keck Baryonic Structure Survey (KBSS; Trainor & Steidel 2012), for which galaxies are originally identified by $U_n G \mathcal{R}$ color selection down to $\mathcal{R} = 25.5$ and spectroscopically confirmed to lie at $z \sim 2$–3 using Keck/LRIS rest-UV spectroscopy (Adelberger et al. 2004; Steidel et al. 2004). As discussed by Conroy et al. (2008), these galaxies are expected to typically evolve into $\sim L^*$ systems by the present day.

Of the few thousand galaxies in KBSS, 306 lie within ~ 1 arcmin of the line of sight to bright background QSOs and have rest-frame optical imaging data obtained using *Hubble Space Telescope* Wide-field Camera 3 (*HST*/WFC3) as a part of Cycle 17 program GO 11694 (PI: Law). The details of these observations have been described at length by Law et al. (2012b). In brief, we used the F160W ($\lambda_{eff} = 15369$ Å) filter to trace rest-frame optical emission from the target galaxies;

these data reach a depth of 27.9 AB for a 5σ detection within a 0.2 arcsec radius aperture and have a typical point-spread function (PSF) FWHM of 0.18 arcsec (corresponding to 1.5 kpc at $z \sim 2$).

We selected galaxies visually classified by Law et al. (2012b) as "Type II," for which the rest-optical morphology consists of two or more distinct nucleated sources of comparable (<10:1) H_{160} magnitude and little to no evidence for extended low surface brightness features connecting the two components (hence reducing the likelihood of multiple clumps within a single low surface-brightness disk; e.g., Genzel et al. 2011; Guo et al. 2012). This selection resulted in 56 galaxies, which we further restricted to the subset with secure redshifts in the range $z = 2.00$–2.65 for which Hα emission lies in the K band between strong atmospheric absorption bands. Additionally, we restricted our sample to galaxies with pair separations greater than 0.5 arcsec (the minimum separation at which we can distinguish objects in seeing-limited follow-up spectroscopy) and less than 2 arcsec (the approximate limit beyond which objects can be unambiguously separated in the ground-based photometry that forms the backbone of the KBSS sample and would have been classified as two separate galaxies). We also rejected targets whose Hα emission was expected to lie extremely close to a bright night-sky emission-line feature. In total, seven galaxies met our combined selection criteria for the 2012A observing season, of which we were able to observe six targets in the available time.

The morphologies of these six galaxies are shown in Figures 1–4; we label the primary, secondary, and, if appropriate, tertiary pieces as "1," "2," and "3," respectively.[6] Assuming that the H_{160} magnitude of these pieces is a proxy for their total stellar mass, we estimate that the mass ratio of these mergers ranges from 1:1 to ~ 8:1 (see Table 1).

As described by Law et al. (2012b), H_{160} magnitudes for these galaxies have been combined with ground-based optical imaging (and in some cases ground-based J, K infrared imaging and/or *Spitzer*/IRAC photometry) to produce stellar population synthesis models of their spectral energy distribution (SED). The photometry used in these models encompasses the light from all components of a given galaxy,[7] and H_{160} magnitudes have been corrected for nebular line emission (see details in Law et al. 2012b). To fit the galaxy SEDs, we use Charlot & Bruzual (CB13) models in combination with a Chabrier (2003) initial mass function and a constant star formation history.

3. SPECTROSCOPIC OBSERVATIONS

We obtained spectroscopic observations of these six galaxies using the Keck/NIRSPEC long-slit spectrograph (McLean et al. 1998) with the slit rotated to lie along the position angle separating the two components visible in the *HST* imaging. Operating in low-resolution mode, the NIRSPEC slit measures 42×0.76 arcsec, with a spectral resolution $R \sim 1400$ as measured from the widths of skylines, and a detector scale

---

[5] All magnitudes are given in AB units unless otherwise noted.

[6] Note that primary, secondary, and tertiary features are generally labeled corresponding to their proximity to the centroid of the ground-based object detections and do not necessarily correspond with the H_{160} magnitude.

[7] Although this may bias the SED fit if the two components are unrelated, the ground-based imaging that provides the rest-UV photometry is neither deep enough nor of sufficiently high resolution to reliably determine magnitudes for individual components visible in the *HST* imaging data. This limitation likewise precludes us from using photometric redshift estimates to identify probable false pairs (e.g., Kartaltepe et al. 2007; Bundy et al. 2009).
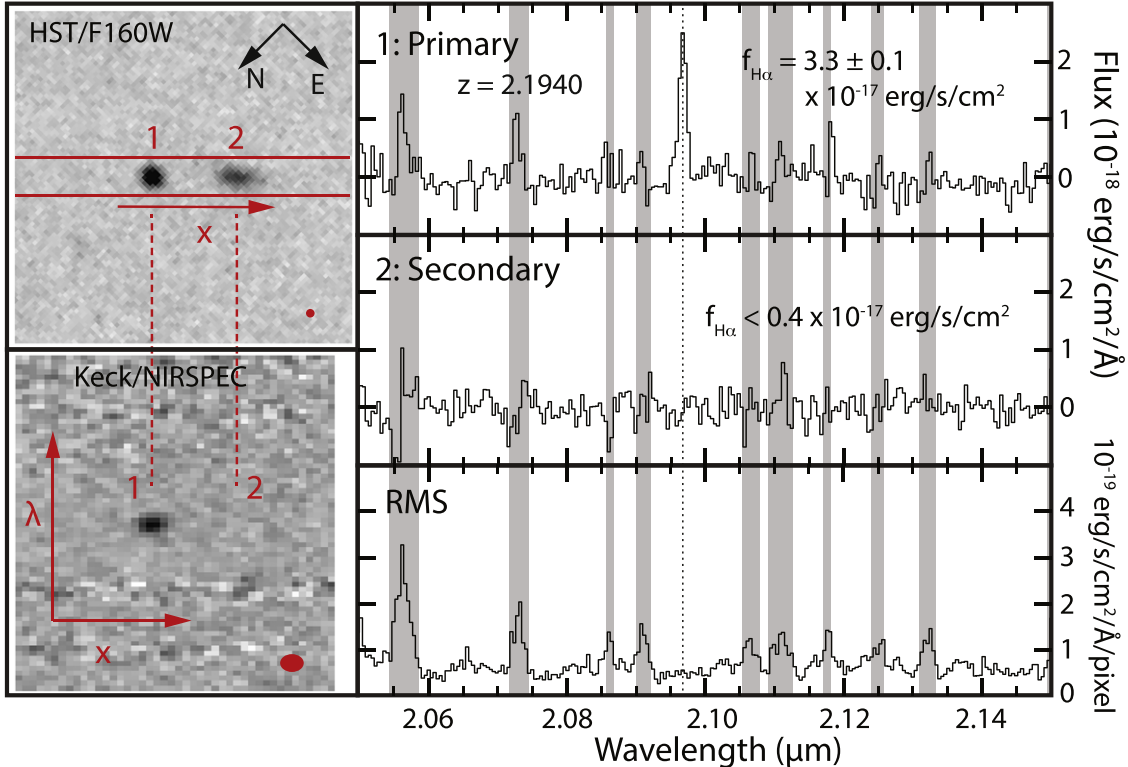
Q1217-BX116

Figure 1. Top left panel: *HST*/F160W imaging data for Q1217-BX116 ($z = 2.19$); panel measures 7×7 arcsec^2. The color map has been inverted and uses an arcsinh stretch with the black point set to 28.46 AB pixel^{-1} (23.0 AB arcsec^{-2}). The orientation of the NIRSPEC slit is indicated by parallel red lines. Bottom left panel: cutout of Keck/NIRSPEC 2d spectrum showing the corresponding spatial region along the slit and ± 2000 km s^{-1} in the wavelength dimension. The colormap has been inverted and uses a linear stretch. Individual components are numbered in both panels, and the red circle in each panel indicates the FWHM of the observational PSF. Right panels: spectra of the primary and secondary objects along with the associated rms noise spectrum; gray shaded bars indicate the wavelengths of strong night-sky OH emission features.

measuring 0.143 arcsec pixel^{-1} along the slit and 4.2 Å pixel^{-1} in the dispersion direction. Integration times were typically 1 hour per target (see Table 2), composed of four 15-minute exposures between which the target galaxy was dithered along the slit. Each target was acquired by blind offsets from a nearby reference star using astrometry derived from the *HST* imaging data.

Five of the six targets (Table 2) were observed on 2012 June 14 in nearly photometric conditions with near-IR K-band seeing ~0.5 arcsec FWHM. In addition, one target (Q2343-BX429) was included from previous observations taken in 2003 September under similar observing conditions that serendipitously had the long slit aligned with the pair separation axis to within 19° (sufficient to incorporate both pieces of the system).

We reduced the spectroscopic data using a hybrid scheme described by Kulas et al. (2012) that includes cosmic-ray rejection, image rectification, and a two-dimensional sky subtraction algorithm (G. Becker 2015, private communication) to model the bright OH night-sky emission lines. The resulting sky-subtracted spectra are stacked, wavelength calibrated to the heliocentric vacuum rest-frame using the OH emission-line features, and flux calibrated using observations of the A0 infrared standard stars HD 1160, HD 203856, and HD 18881 (Vega magnitudes $K = 7.04$, 6.84, and 7.14, respectively). Two-dimensional reduced spectra (i.e., slit direction along the abscissa and spectral direction along the ordinate) for each of the target galaxies are shown in Figures 1–

4. Except where noted otherwise, we extract spectra of the primary, secondary, and (where applicable) tertiary objects using a 1 arcsec (7 pixel) wide box and construct a noise spectrum for each target by measuring the rms variations in a similar box along blank regions of the slit.

4. RESULTS

We show the *HST*/F160W morphologies and NIRSPEC spectra for our six target galaxies in Figures 1–4, along with estimates of the rms noise spectrum for each galaxy. The sensitivity of these spectra is a function of wavelength; using the rms spectra constructed from blank-sky regions for each galaxy, we estimate that the 3σ limit on spatially and spectroscopically unresolved emission ranges from 4×10^{-18} erg s^{-1} cm^{-2} at $\lambda = 2.1$ μm to $\sim 2 \times 10^{-17}$ erg s^{-1} cm^{-2} at $\lambda = 2.4$ μm where the thermal background of the Keck/NIRSPEC system becomes large. We estimate the uncertainty in central wavelength and FWHM of individual lines from bootstrapped Monte Carlo tests in which realizations of the noise defined by the rms spectra have been added to the object spectra. We compute the velocity dispersion σ_v of each target by subtracting off the instrumental resolution in quadrature from the measured FWHM of the Hα emission line, and estimate the spatial effective radius of nebular line emission along the slit by fitting a Gaussian profile, subtracting the $0\farcs5$ seeing in quadrature from the measured Gaussian FWHM, and dividing by 2.36 to obtain the effective 1σ radius.
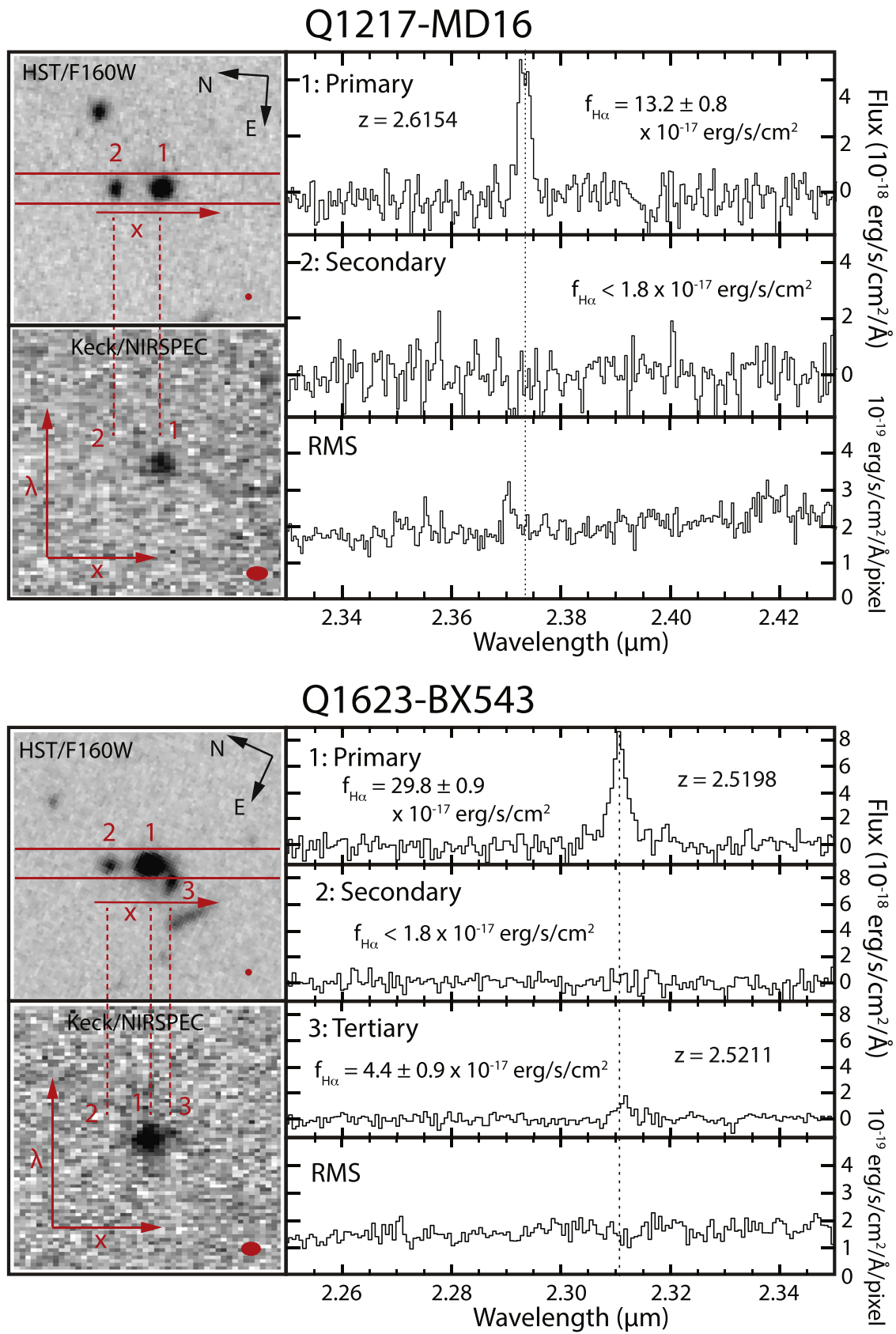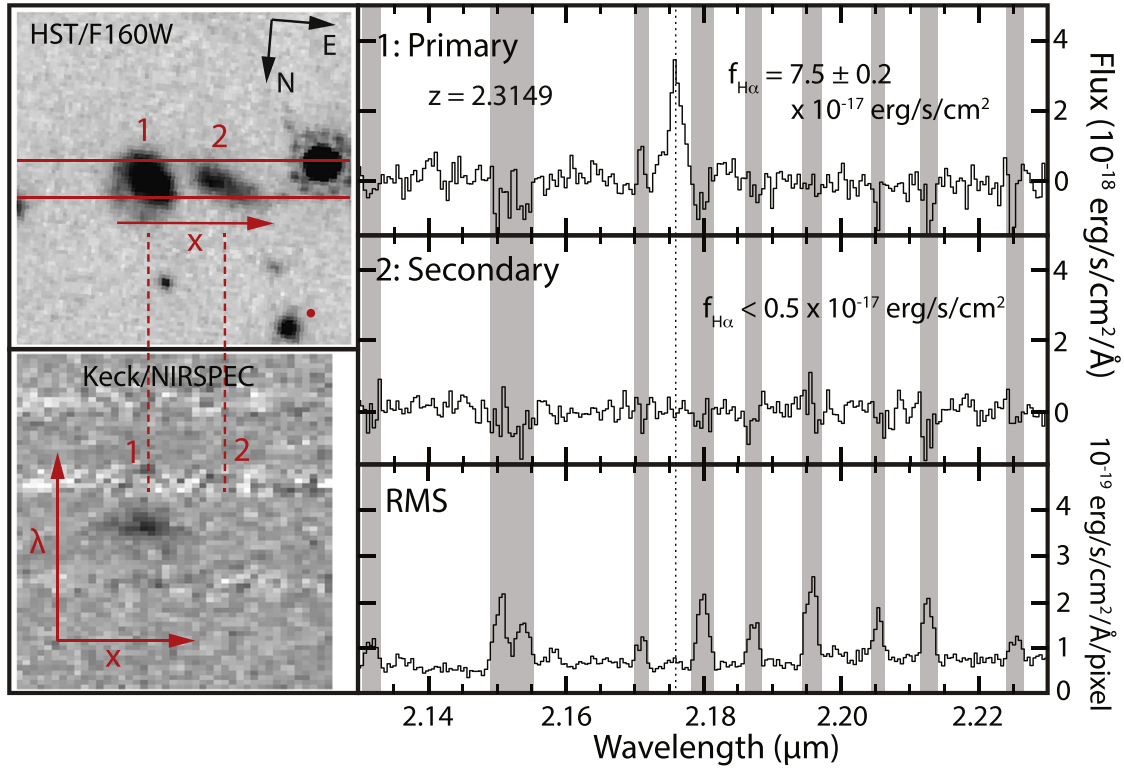
Figure 2. Same as Figure 1, but for Q1217-MD16 and Q1623-BX543 ($z = 2.62$ and 2.52, respectively). The NIRSPEC spectra for Q1623-BX543 show the tertiary component, visible in the bottom left panel as a small spoke extending to the top right of the primary component.
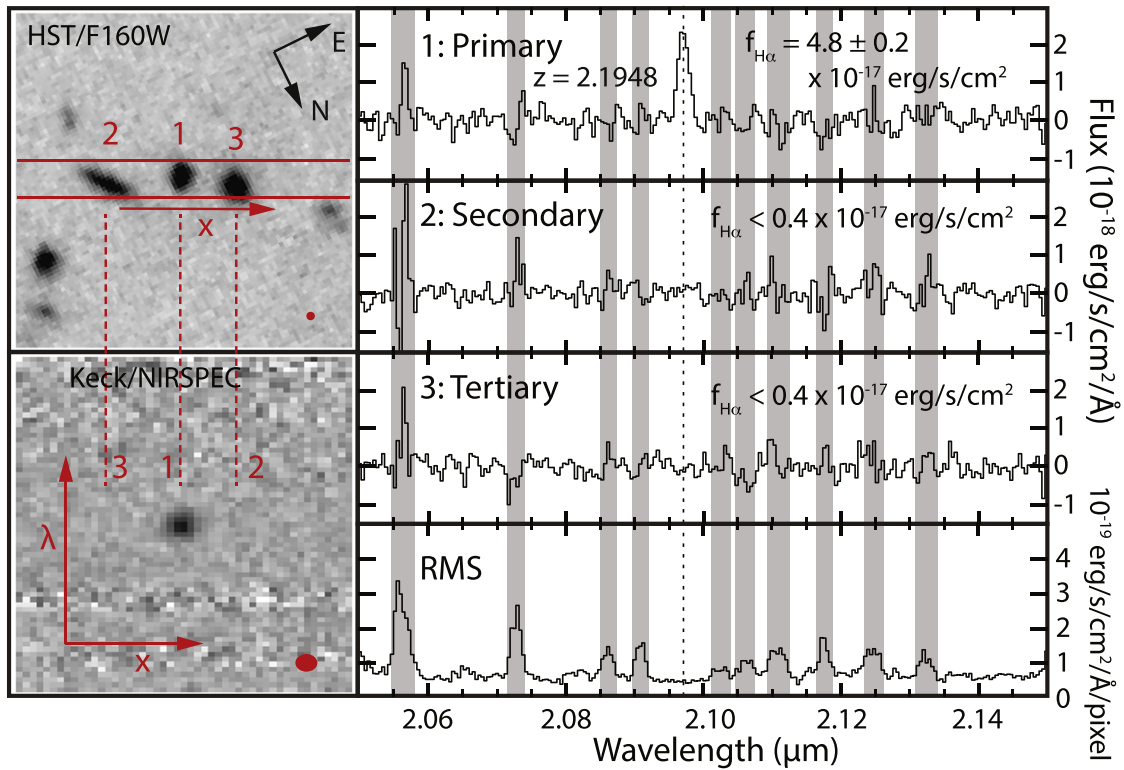
Q1700-MD103

Q2206-BM64

Figure 3. Same as Figure 1, but for Q1700-MD103 and Q2206-BM64 ($z = 2.31$ and 2.19, respectively). The object on the eastern end of the Q1700-MD103 slit is a foreground star.
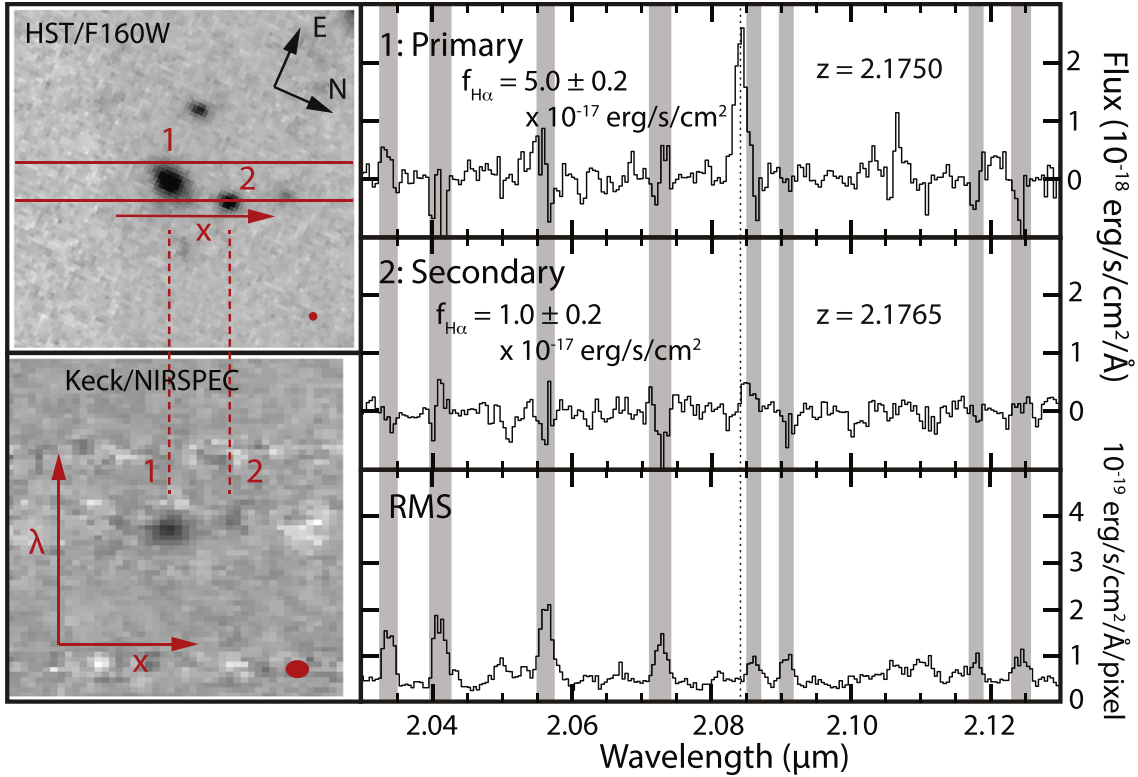
Q2343-BX429

Figure 4. Same as Figure 1, but for Q2343-BX429 ($z = 2.17$).

Table 1
Target Galaxies

Galaxy	R.A.[a] (J2000)	Decl.[a] (J2000)	Secondary Distance[b] (kpc)	Tertiary Distance[c] (kpc)	H_{160} (Primary)	Secondary Mass Ratio[d]	Tertiary Mass Ratio[d]
Q1217-BX116	12:19:31.271	+49:41:21.90	14	⋯	24.56	1:1	⋯
Q1217-MD16	12:19:28.407	+49:40:50.15	9	⋯	23.44	4:1	⋯
Q1623-BX543	16:25:57.736	+26:50:09.44	9	7	22.82	8:1	5:1
Q1700-MD103	17:01:00.321	+64:11:55.42	13	⋯	22.51	2:1	⋯
Q2206-BM64	22:08:52.360	−19:43:28.27	10	13	24.03	1:1	1:1
Q2343-BX429	23:46:22.968	+12:49:05.55	10	⋯	24.71	7:1	⋯

Notes.
[a] Coordinates represent the approximate point midway between the components based on the *HST*/WFC3 imaging data.
[b] Projected distance of secondary from the primary source.
[c] Projected distance of tertiary from the primary source.
[d] Estimated from the ratio of H_{160} magnitudes.

4.1. Q1217-BX116

Q1217-BX116 appears to be a relatively isolated double system in which both components have similar H-band magnitudes ($H_{160} = 24.56$ for the primary component, and 24.74 for the secondary component) and are separated by $1\rlap{.}''7$ in projection (corresponding to 14 kpc at $z = 2.19$). The secondary component has a circularized effective radius $r_e = 1.4$ kpc, significantly more elongated than the primary ($r_e < 0.6$ kpc).[8] Based on SED modeling, Q1217-BX116 is young (202 Myr) and low mass ($M_* = 2.4 \times 10^9 M_\odot$) with an

SFR of 11 $M_\odot$ yr^{-1}. Previous rest-UV spectroscopy obtained with Keck/LRIS (see, e.g., Steidel et al. 2010 and references therein) serendipitously included both pieces of the galaxy and showed extremely strong Lyα emission with no clear absorption features.

The primary component of the pair is detected in Hα to high confidence in our long-slit NIRSPEC spectroscopy with an observed flux of $(3.3 \pm 0.1) \times 10^{-17}$ erg s^{-1} cm^{-2}. As indicated by Figure 1 (bottom left panel), there is no evidence of a tilt in the Hα emission profile, which has a roughly Gaussian profile along the spatial direction with an FWHM $0\rlap{.}''44$ (i.e., consistent with an unresolved point source with an intrinsic effective radius of $r_{H\alpha} < 1.2$ kpc given the $\sim 0\rlap{.}''5$ seeing) and is spectrally unresolved with $\sigma_v < 91$ km s^{-1}. Despite the strong detection of the primary in the middle of a relatively OH-free spectral region ~ 700 km s^{-1} wide, there is no evidence of Hα

---

[8] Circularized effective radii are derived using GALFIT (Peng et al. 2002) and a model of the *HST*/WFC3 PSF and converted to kiloparsecs assuming that both pieces lie at the systemic redshift of the galaxy. As detailed in Law et al. (2012b), radii are likely systematically underestimated for sources with $H_{160} > 24$ AB.

Table 2
Galaxy Emission Properties

Galaxy	$z_{H\alpha}$	$\lambda_{H\alpha}$ (Å)	Primary Flux (10^{-17} erg s^{-1} cm^{-2})	Primary σ_v (km s^{-1})	Secondary (Tertiary) Flux[a] (10^{-17} erg s^{-1} cm^{-2})	SLITPA[b]	$N_{\exp}$[c]
Q1217-BX116	2.1940	20967.5 ± 0.2	3.3 ± 0.1	<91	<0.4	$135°$	4
Q1217-MD16	2.6154	23733.6 ± 0.8	13.2 ± 0.8	103 ± 13	<1.8	$184°$	4
Q1623-BX543	2.5198	23105.8 ± 0.7	26.8 ± 0.9	180 ± 8	<1.8 (4.4 ± 0.9)	$205°$	3
Q1700-MD103	2.3149	21760.7 ± 0.5	7.5 ± 0.2	102 ± 12	<0.5	$95°$	5
Q2206-BM64	2.1948	20972.4 ± 0.1	4.8 ± 0.2	64 ± 4	<0.4 (<0.4)	$64°$	5
Q2343-BX429	2.1750	20842.4 ± 0.2	5.0 ± 0.2	66 ± 7	1.0 ± 0.2	$24°$	4

Notes.
[a] Flux limits are 3σ limits for a spectroscopically unresolved feature at the wavelength of Hα emission for the primary object. Tertiary fluxes or flux limits are only given where applicable.
[b] Degrees east of north.
[c] Exposure time is $N \times 900$ s.

emission from the secondary component. If the secondary component is not an unrelated interloper along the line of sight to Q1217-BX116, we can use the rms noise spectrum to place a 3σ upper limit of 4×10^{-18} erg s^{-1} cm^{-2} on the Hα emission flux from a spatially and spectroscopically unresolved source (i.e., roughly 10 times fainter than the primary).

4.2. Q1217-MD16

The two morphological components of Q1217-MD16 differ by a factor of 3.8 in brightness ($H_{160} = 23.44$ and 24.89 for the primary/secondary components, respectively) and are separated by $1''.1$ (9 kpc at $z = 2.62$). The primary and secondary components have similar circularized effective radii of $r_e = 0.6$ and 0.7 kpc, respectively. Similar to Q1217-BX116, SED models indicate that Q1217-MD16 is relatively young (80 Myr) and low mass ($M_* = 7 \times 10^9 M_\odot$) with an SFR of $88 \, M_\odot \, \mathrm{yr}^{-1}$. Previous Keck/LRIS rest-UV spectroscopy obtained at three different position angles suggested two components as the interstellar absorption line features at $z = 2.609$ and $z = 2.616$, along with Lyα emission at $z = 2.624$.

As indicated by Figure 2, the primary component is well detected in Hα at $z = 2.6154$ with flux $(13.2 \pm 0.8) \times 10^{-17}$ erg s^{-1} cm^{-2}, consistent with recent Keck/MOSFIRE spectroscopy (C.C. Steidel et al. 2015, in preparation), which detected Hβ emission at a redshift of $z = 2.6168$. Although the nebular emission is spatially unresolved ($r_{H\alpha} < 1.2$ kpc after accounting for the observational see-ing), it has a velocity dispersion of $\sigma_v = 103 \pm 13 \, \mathrm{km \, s}^{-1}$. Despite the suggestion of a two-component system from the rest-UV spectroscopy, no Hα emission is detected at the location of the secondary morphological feature to a 3σ limit of 1.8 ± 10^{-17} erg s^{-1} cm^{-2}.

4.3. Q1623-BX543

Q1623-BX543 is a complicated system with three distinct morphological components within ~ 1 arcsec of each other (Figure 2) and magnitudes $H_{160} = 22.82$, 25.12, and 24.48 for the primary, secondary, and tertiary components. respectively. The circularized effective radius of the primary component is 0.9 kpc, comparable to the secondary and tertiary features. SED models indicate that Q1623-BX543 is young (9 Myr), low

mass ($M_* = 5 \times 10^9 M_\odot$), and forming stars extremely rapidly at a rate of 515 $M_\odot \, \mathrm{yr}^{-1}$ (see the discussion in Section 5).

Previous H-band observations of Q1623-BX543 with adaptive-optics-assisted OSIRIS integral-field spectroscopy (Law et al. 2009) found that components 1 and 3 are physically associated, with [O III] emission features offset from each other by 125 km s^{-1} in velocity and 6.7 kpc ($0''.8$) in projected separation. The present NIRSPEC observations indicate that the primary component has an effective Hα radius of $\sim 1.2 \pm 0.3$ kpc[9] and a broad velocity dispersion of $\sigma_v = 180 \pm 8$ km s^{-1} with no apparent rotation about a pre-ferred kinematic axis. Given the lower spectral and spatial resolution of the NIRSPEC data, the measured size and kinematics are fairly consistent with the OSIRIS [O III] $\lambda5007$ observations ($R \sim 3400$, PSF FWHM $\sim 0''.15$), which suggested that this component has an effective radius of 1.1 $\pm$ 0.1 kpc and a net velocity dispersion of $\sigma_v = 153 \pm 7$ km s^{-1}.[10]

Although the NIRSPEC long-slit observations were not intended to measure the properties of the tertiary component (the position angle of the slit was chosen to cover the primary and secondary components), we nonetheless detect the tertiary feature at $0''.5$ projected distance along the slit. Extracting the spectrum from this location gives a flux of $(4.4 \pm 0.9) \times 10^{-17}$ erg s^{-1} cm^{-2}, which is offset from the primary by 120 $\pm$ 30 km s^{-1}, consistent with the 125 km s^{-1} derived from the OSIRIS [O III] observations. The tertiary feature is too faint to obtain a reliable estimate of its velocity dispersion, but our derived value ($\sigma_v = 110^{+40}_{-70}$ km s^{-1}) is consistent with previous OSIRIS [O III] estimates of $\sigma_{mean} = 60 \pm 10$ km s^{-1}. We note that the dynamical mass ratio (8:1) of these two components as derived from the OSIRIS data is consistent with the stellar mass ratio estimated using the H_{160} magnitude (5:1; see Table 1).

The secondary morphological component located $1''.1$ (9 kpc) in projection to the northeast of the primary was not covered by the previous OSIRIS IFU data. While the successful re-detection of the tertiary component gives us confidence in the ability of the NIRSPEC observations to discern faint features down to small angular separations, as indicated by

---

[9] Uncertainty is dominated by the uncertainty in the observational PSF.
[10] These are estimates of the integrated line width from the composite spectrum of the galaxy; the OSIRIS data demonstrate that the galaxy has a mean internal velocity dispersion of $\sigma_{mean} = 139$ km s^{-1} (rms = 32 km s^{-1}), with a velocity shear of 39 $\pm$ 4 km s^{-1}.

Figure 2, we detect no Hα emission from the secondary component to a 3σ limit of $1.8 \times 10^{-17}\,\mathrm{erg\,s^{-1}\,cm^{-2}}$.

4.4. Q1700-MD103

Q1700-MD103 is significantly larger than most of the other galaxies, with primary (secondary) magnitude $H_{160} = 22.51$ (23.33) and circularized effective radius $r_e = 3.0$ (2.7) kpc. The secondary morphological component is highly elongated with a centroid located $1\!''\!.5$ east of the primary in projection (13 kpc at $z = 2.31$). Given the large effective radius of the primary, it is unsurprising that the best-fit SED for the galaxy corresponds to an old (1 Gyr) and massive ($M_* = 5 \times 10^{10} M_\odot$) stellar population with an ongoing SFR of 49 $M_\odot\,\mathrm{yr^{-1}}$.

Q1700-MD103 has strong Hα emission, with a flux from the primary component of $(7.5 \pm 0.2) \times 10^{-17}\,\mathrm{erg\,s^{-1}\,cm^{-2}}$. While the galaxy is a good candidate for rotation given its high mass (see, e.g., Förster Schreiber et al. 2009; Law et al. 2009; Newman et al. 2013), no rotation is evident along the axis traced by the NIRSPEC slit. Rather, it has an instrumentally deconvolved velocity dispersion $\sigma_v = 102 \pm 12\,\mathrm{km\,s^{-1}}$ and a large Hα profile of effective radius 2.5 ± 0.2 kpc that roughly matches its rest-optical continuum radius.

In contrast, there is no trace of Hα emission from the secondary component to a 3σ limit of $5 \times 10^{-18}\,\mathrm{erg\,s^{-1}\,cm^{-2}}$. In this case, we have the benefit of *HST*/ACS F814W imaging (from program GO-10581; PI: A. E. Shapley) tracing rest-frame $\sim$2500 Å emission at the redshift of the primary component to help us understand this negative result. As shown in Law et al. (2012a, see their Figure 9), the second component is extremely red compared to the primary ($I_{814} - H_{160} = 2.7$ versus 1.3) and only barely detected in the F814W imaging. Since the primary and secondary objects have such different colors, it is probable that they either lie at different redshifts or that the secondary is significantly dustier/older; both explanations are consistent with the lack of detection of Hα.

4.5. Q2206-BM64

Q2206-BM64 is a morphological triple system with magnitudes $H_{160} = 24.03$, 23.67, and 23.89 for the primary, secondary, and tertiary components, respectively; primary–secondary separation of $1\!''\!.1$ (9.7 kpc); and a primary–tertiary separation of $1\!''\!.5$ (12.8 kpc). While the primary and secondary components are relatively circular with effective radii $r_e = 0.8$ and 1.4 kpc, respectively, the tertiary component is highly elongated with $r_e = 1.3$ kpc. Q2206-BM64 has an SED best fit with a relatively old (806 Myr) and massive ($M_* = 3 \times 10^{10} M_\odot$) stellar population and 37 $M_\odot\,\mathrm{yr^{-1}}$ of ongoing star formation.

The unusual configuration of all three clumps in a nearly straight line meant that it was possible to obtain NIRSPEC spectroscopy of all three components simultaneously. Although all three have similar colors based on our marginally resolved multi-wavelength ground-based imaging, as indicated in Figure 4, only the primary component is detected in Hα emission with a flux of $(4.8 \pm 0.2) \times 10^{-17}\,\mathrm{erg\,s^{-1}\,cm^{-2}}$. While the emission from the primary is spatially unresolved (effective radius $\lesssim 1.2$ kpc), it has a velocity dispersion of $\sigma_v = 64 \pm 4\,\mathrm{km\,s^{-1}}$.

4.6. Q2343-BX429

Q2343-BX429 is composed of two clumps of magnitude $H_{160} = 24.71$ and 26.83 for the primary and secondary pieces, respectively, with a projected separation of $1\!''\!.2$ (10 kpc at $z = 2.17$). The primary component has an effective radius $r_e = 1.5$ kpc, while the secondary component is spatially unresolved with $r_e \leqslant 0.6$ kpc. Similarly to Q1700-MD103 and Q2206-BM64, the SED of Q2343-BX429 is most consistent with an old (1.1 Gyr) and relatively massive ($M_* = 2 \times 10^{10} M_\odot$) stellar population, with a small ongoing SFR of 14 $M_\odot\,\mathrm{yr^{-1}}$.

By coincidence, Q2343-BX429 was observed in 2003 July using Keck/NIRSPEC with the same instrumental setup and similar K-band seeing ($0\!''\!.5$) as the rest of our galaxy targets and with a position angle sufficiently close to the separation vector between the two morphological components that both fell within the spectroscopic slit. The original reduction and analysis of these data have been described by Erb et al. (2004, 2006). As illustrated in Figure 4, both the primary and secondary components are detected in the long-slit spectra. The primary component has a measured Hα flux of $(5.0 \pm 0.2) \times 10^{-17}\,\mathrm{erg\,s^{-1}\,cm^{-2}}$ with an effective radius < 1.2 kpc and a velocity dispersion $\sigma_v = 66 \pm 7\,\mathrm{km\,s^{-1}}$. Although the secondary component is faint (Hα flux $(1.0 \pm 0.2) \times 10^{-17}\,\mathrm{erg\,s^{-1}\,cm^{-2}}$), it is centered on exactly the location expected from the broadband *HST*/F160W imaging data and has a centroid offset from the primary by $140 \pm 30\,\mathrm{km\,s^{-1}}$. While this secondary component can be detected, we note that its flux calibration has a systematic uncertainty (of roughly a factor of two) compared to the primary component since it lies on the edge of the spectrograph slit. It is also too faint, and too close, to an OH skyline to obtain a reliable estimate of the intrinsic velocity dispersion.

5. DISCUSSION

On the whole, the Hα-derived properties of the target galaxies match well with expectations based on *HST*/WFC3 imaging and broadband photometry. As indicated by Table 3, the Hα and rest-optical continuum radii are consistent with each other to within $\sim$20%, indicating that the ongoing star formation is spatially coincident with the stellar mass accumulated during past star formation episodes. This result is limited by our inability to measure true two-dimensional profiles from the long-slit data, but is consistent with previous findings from studies of $z \sim 2$ star-forming galaxies using adaptive-optics-assisted integral field spectroscopy (e.g., Law et al. 2009; Förster Schreiber et al. 2011).

Similarly, the SFR derived from Hα emission-line flux and global SED modeling are in reasonable agreement. We estimate the SFR from the Hα luminosity using the relation from Kennicutt et al. (1994) combined with a Chabrier (2003) initial mass function and an extinction correction based on the Calzetti et al. (2000) law (see discussion by Erb et al. 2012; Reddy et al. 2012) and the SED derived $E(B - V)$. As shown in Table 3, extinction-corrected Hα and SED-based star formation estimates generally agree to within a factor of $\sim$2 or better. The sole exception (Q1623-BX543) has a formal best-fit stellar population age of less than 50 Myr, which is known to significantly inflate estimates of the SFR above other indicators (Reddy et al. 2012).

Table 3
Galaxy Properties

Galaxy	r_e [a] (kpc)	$r_{H\alpha}$ [b] (kpc)	$E(B-V)$	M_* ($10^9 M_\odot$)	$SFR_{H\alpha}$ [c] ($M_\odot$ yr^{-1})	SFR_{SED} ($M_\odot$ yr^{-1})	SFR_{Comp} [d] ($M_\odot$ yr^{-1})
Q1217-BX116	1.4	<1.2	0.17	2.4	9 ± 1	11	<1
Q1217-MD16	0.6	<1.2	0.21	7.0	62 ± 4	88	<9
Q1623-BX543	0.9	1.2 ± 0.3	0.30	5.0	158 ± 5	515	23 ± 5
Q1700-MD103	3.0	2.5 ± 0.2	0.28	50	34 ± 1	49	<2
Q2206-BM64	0.8	<1.2	0.21	30	15 ± 1	37	<1
Q2343-BX429	1.5	<1.2	0.18	20	14 ± 1	14	3 ± 1

Notes.
[a] PSF-corrected circularized effective radius of the primary component derived from *HST*/WFC3 broadband imaging. See Law et al. (2012b) for a discussion of typical uncertainties.
[b] PSF-corrected Gaussian half-light radius of the primary component derived from Keck/NIRSPEC Hα profile along the spectroscopic slit.
[c] Extinction-corrected estimate for the primary component. Uncertainties represent statistical uncertainty in the Hα flux measurement and do not incorporate systematic uncertainty in the SFR prescription adopted.
[d] Extinction-corrected estimate for the morphological secondary companion (tertiary source for Q1623-BX543).

Of the six galaxies observed, two were confirmed to have nearby companions (Q1623-BX543, Q2343-BX429; mass ratios 5:1 and 7:1, respectively) whose projected separations and relative velocities indicate that they are likely in the process of merging with the central galaxy.[11] As indicated by Figure 5, all six primary objects and both confirmed companions lie near the star-forming galaxy main sequence for $z = 1.5$–2.5 galaxies (e.g., Wuyts et al. 2011). This pair confirmation rate (1/3) is consistent with the expectation that ~1/2 of apparent pairs with angular separations ~1–2 arcsec are physically unrelated superpositions along the line of sight based on the statistical distribution of sources in the *HST*/WFC3 imaging fields (see the discussion by Law et al. 2012b). This explanation is perhaps particularly likely for Q1700-MD103 and Q2206-BM64, for which the putative companions fall well below the star formation main sequence (lower right open triangles in Figure 5). However, our results are also compatible with the hypothesis that the SFR in merging pairs can differ by a factor of 10 between each of the components, even when the components have similar rest-optical continuum magnitudes. Such an explanation was recently put forward by Schmidt et al. (2013), who used 3D-*HST* grism spectroscopy to show that apparent morphological pairs tended to have nebular emission-line indicators of star formation concentrated in just one component of the pair, ascribing the difference to different gas content in the components of the merger. Here, we push the SFR threshold required for detection an order of magnitude deeper than Schmidt et al. (2013), but similarly find an absence of evidence for pronounced star formation in the merging companions.

In previous analyses of the $z \sim 2$ star-forming galaxy population, we found (Law et al. 2007a, 2012b, 2012c) that rest-frame UV and optical continuum morphology was largely decoupled from other physical properties, with merger-like galaxies having a distribution of stellar masses and SFRs statistically consistent with the non-merger population. However, as discussed by Law et al. (2012b), apparent morphological pairs tended to have marginally higher SFR surface density than the rest of the $z \sim 2$ star-forming galaxy
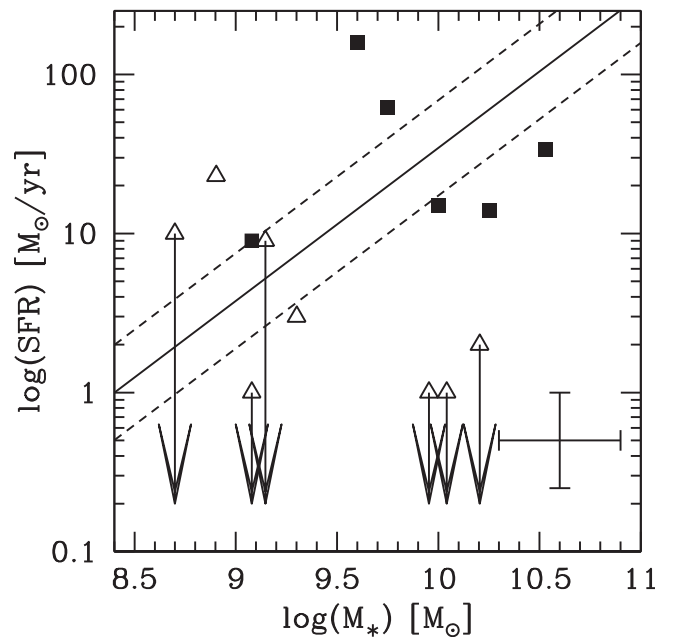

Figure 5. Estimated stellar mass and SFR for the primary (filled squares) and secondary/tertiary (filled triangles) objects. Stellar masses are estimated from the best-fit stellar population model of the integrated light of the system (divided up between components according to their relative H_{160} flux); SFRs are derived from the nebular emission-line fluxes and upper limits. The error bar in the lower right corner of the panel indicates the typical uncertainty of a given point (which is dominated by systematics). The solid line represents the track of the star-forming galaxy main sequence at $z = 1.5$–2.5 taken from Wuyts et al. (2011); dashed lines indicate an SFR a factor of two above and below this track.

population ($\langle \Sigma_{SFR} \rangle = 10$ $M_\odot$ yr^{-1} kpc^{-2} for mergers versus 4 $M_\odot$ yr^{-1} kpc^{-2} for non-mergers, with 0.2% confidence in the null hypothesis being drawn from the same distribution). Additionally, such pairs were much more likely to show Lyα in emission than the rest of the galaxy sample, with many of the strongest Lyα sources (e.g., Q1217-BX116) having a double-component morphology (Law et al. 2012c). This latter trend was also noted by Cooke et al. (2010), whose study of spectroscopically confirmed Lyman Break Galaxy pairs at $z \sim 3$ found that pairs were much more likely than non-pairs to exhibit Lyα in emission (although, cf. Shibuya et al. 2014).

---

[11] Although, as discussed by Patton & Atfield (2008) and Lotz et al. (2011), even close pairs with similar spectroscopic redshifts are not *certain* to be merging systems since small redshift differences can correspond to large separations along the line of sight.

While it is impossible to draw statistically robust conclusions from our small pilot sample, it is nonetheless informative to consider how the properties of our two spectroscopic pairs compare to those of the overall star-forming galaxy population from which they were drawn ($\langle M_\odot \rangle \sim 10^{10} M_\odot$, $\langle \mathrm{SFR} \rangle \sim 30\ M_\odot\ \mathrm{yr}^{-1}$; see Figure 18 of Law et al. 2012b). As detailed in Sections 4.3 and 4.6 above, Q1623-BX543 has a higher than average SFR and Σ_{SFR} and lower than average stellar mass and circularized effective radius. In contrast, Q2343-BX429 has a lower than average SFR, higher than average stellar mass, and r_e and Σ_{SFR} fairly typical of the $z \sim 2$ star-forming galaxy population. Neither galaxy shows Lyα in emission based on rest-frame UV spectra. Although our findings are therefore marginally inconsistent with the findings of Cooke et al. (2010) and Law et al. (2012c) that merging pairs seem more likely than non-pairs to show Lyα emission, they generally match other findings (Law et al. 2007a, 2012b; Lee et al. 2013; Schmidt et al. 2013) that spectroscopic pairs do not have physical properties any different on average from those of the $z \sim 2$ star-forming galaxy population as a whole.

Looking forward, we note that it will soon be possible to resolve such discrepancies. Using catalogs of close-pair candidates extracted from large-area morphological surveys such as CANDELS and high-sensitivity follow-up spectroscopy using recently commissioned multi-object NIR spectrographs such as MOSFIRE (e.g., Kriek et al. 2014) and KMOS (e.g., Wisnioski et al. 2014) is likely to spectroscopically confirm samples of a few tens to hundreds of genuine mergers for only a modest investment in observing time. Such statistically large, representative samples will allow us to determine the influence of major merging events on the evolution of gas and stellar populations in galaxies in the young universe.

REFERENCES

Adelberger, K. L., Steidel, C. C., Shapley, A. E., et al. 2004, ApJ, 607, 226
Bournaud, F., & Elmegreen, B. G. 2009, ApJL, 694, L158
Bruzual, G., Charlot, S., Lópezlira, R. G., et al. 2013, in IAU Symp. 295, The Intriguing Life of Massive Galaxies (Paris: IAU), 282
Bundy, K., Fukugita, M., Ellis, R. S., et al. 2009, ApJ, 697, 1369
Calzetti, D., Armus, L., Bohlin, R. C., et al. 2000, ApJ, 533, 682
Chabrier, G. 2003, PASP, 115, 763
Chou, R. C. Y., Bridge, C. R., & Abraham, R. G. 2012, ApJ, 760, 113
Conroy, C., Shapley, A. E., Tinker, J. L., Santos, M. R., & Lemson, G. 2008, ApJ, 679, 1192
Conselice, C. J. 2014, ARA&A, 52, 291
Conselice, C. J., Bershady, M. A., & Jangren, A. 2000, ApJ, 529, 886
Conselice, C. J., Bluck, A. F. L., Ravindranath, S., et al. 2011, MNRAS, 417, 2770
Conselice, C. J., Rajgor, S., & Myers, R. 2008, MNRAS, 386, 909
Cooke, J., Berrier, J. C., Barton, E. J., Bullock, J. S., & Wolfe, A. M. 2010, MNRAS, 403, 1020
Dekel, A., Birnboim, Y., Engel, G., et al. 2009, Natur, 457, 451
de Ravel, L., le Fèvre, O., Tresse, L., et al. 2009, A&A, 498, 379
Erb, D. K., Quider, A. M., Henry, A. L., & Martin, C. L. 2012, ApJ, 759, 26
Erb, D. K., Steidel, C. C., Shapley, A. E., Pettini, M., & Adelberger, K. L. 2004, ApJ, 612, 122
Erb, D. K., Steidel, C. C., Shapley, A. E., et al. 2006, ApJ, 647, 128
Förster Schreiber, N. M., Genzel, R., Bouché, N., et al. 2009, ApJ, 706, 1364
Förster Schreiber, N. M., Shapley, A. E., Erb, D. K., et al. 2011, ApJ, 731, 65
Genzel, R., Burkert, A., Bouché, N., et al. 2008, ApJ, 687, 59
Genzel, R., Newman, S., Jones, T., et al. 2011, ApJ, 733, 101
Guo, Y., Giavalisco, M., Ferguson, H. C., Cassata, P., & Koekemoer, A. M. 2012, ApJ, 757, 120
Kartaltepe, J. S., Sanders, D. B., Scoville, N. Z., et al. 2007, ApJS, 172, 320
Kassin, S. A., Brooks, A., Governato, F., Weiner, B. J., & Gardner, J. P. 2014, ApJ, 790, 89
Kaviraj, S., Cohen, S., Windhorst, R. A., et al. 2013, MNRAS, 429, L40
Kennicutt, R. C., Jr., Tamblyn, P., & Congdon, C. E. 1994, ApJ, 435, 22
Komatsu, E., Smith, K. M., Dunkley, J., et al. 2011, ApJS, 192, 18
Kriek, M., Shapley, A. E., Reddy, N. A., et al. 2015, ApJS, 218, 15
Kulas, K. R., Shapley, A. E., Kollmeier, J. A., et al. 2012, ApJ, 745, 33
Law, D. R., Shapley, A. E., Steidel, C. C., et al. 2012a, Natur, 487, 338
Law, D. R., Steidel, C. C., Erb, D. K., et al. 2007a, ApJ, 656, 1
Law, D. R., Steidel, C. C., Erb, D. K., et al. 2007b, ApJ, 669, 929
Law, D. R., Steidel, C. C., Erb, D. K., et al. 2009, ApJ, 697, 2057
Law, D. R., Steidel, C. C., Shapley, A. E., et al. 2012b, ApJ, 745, 85
Law, D. R., Steidel, C. C., Shapley, A. E., et al. 2012c, ApJ, 759, 29
Lee, B., Giavalisco, M., Williams, C. C., et al. 2013, ApJ, 774, 47
Lin, L., Koo, D. C., Willmer, C. N. A., et al. 2004, ApJL, 617, L9
López-Sanjuan, C., Le Fèvre, O., Tasca, L. A. M., et al. 2013, A&A, 553, A78
Lotz, J. M., Jonsson, P., Cox, T. J., & Primack, J. R. 2008, MNRAS, 391, 1137
Lotz, J. M., Jonsson, P., Cox, T. J., & Primack, J. R. 2010, MNRAS, 404, 575
Lotz, J. M., Jonsson, P., Cox, T. J., et al. 2011, ApJ, 742, 103
Lotz, J. M., Primack, J., & Madau, P. 2004, AJ, 128, 163
McLean, I. S., Becklin, E. E., Bendiksen, O., et al. 1998, Proc. SPIE, 3354, 566
Newman, S. F., Genzel, R., Förster Schreiber, N. M., et al. 2013, ApJ, 767, 104
Papovich, C., Dickinson, M., Giavalisco, M., Conselice, C. J., & Ferguson, H. C. 2005, ApJ, 631, 101
Patton, D. R., & Atfield, J. E. 2008, ApJ, 685, 235
Peng, C. Y., Ho, L. C., Impey, C. D., & Rix, H.-W. 2002, AJ, 124, 266
Puech, M., Hammer, F., Rodrigues, M., et al. 2014, MNRAS, 443, L49
Quadri, R. F., & Williams, R. J. 2010, ApJ, 725, 794
Rawat, A., Hammer, F., Kembhavi, A. K., & Flores, H. 2008, ApJ, 681, 1089
Reddy, N. A., Pettini, M., Steidel, C. C., et al. 2012, ApJ, 754, 25
Reddy, N. A., Steidel, C. C., Pettini, M., et al. 2008, ApJS, 175, 48
Schmidt, K. B., Rix, H.-W., da Cunha, E., et al. 2013, MNRAS, 432, 285
Shapiro, K. L., Genzel, R., Förster Schreiber, N. M., et al. 2008, ApJ, 682, 231
Shibuya, T., Ouchi, M., Nakajima, K., et al. 2014, ApJ, 785, 64
Steidel, C. C., Erb, D. K., Shapley, A. E., et al. 2010, ApJ, 717, 289
Steidel, C. C., Shapley, A. E., Pettini, M., et al. 2004, ApJ, 604, 534
Tasca, L. A. M., le Fèvre, O., López-Sanjuan, C., et al. 2014, A&A, 565, A10
Trainor, R. F., & Steidel, C. C. 2012, ApJ, 752, 39
van der Wel, A., Chang, Y.-Y., Bell, E. F., et al. 2014, ApJL, 792, LL6
Williams, R. J., Quadri, R. F., & Franx, M. 2011, ApJL, 738, L25
Wisnioski, E., Förster Schreiber, N. M., Wuyts, S., et al. 2015, ApJ, 799, 209
Wuyts, S., Förster Schreiber, N. M., van der Wel, A., et al. 2011, ApJ, 742, 96